

# Solid-phase structures of the Dzugutov pair potential

J. Roth, Institut für Theoretische und Angewandte Physik, Universität Stuttgart,  
Paffenwaldring 57, 70550 Stuttgart, Germany

A. R. Denton, Department of Physics, Acadia University, Wolfville, NS, Canada B0P 1X0

(February 1, 2008)

## Abstract

In recent computer simulations of a simple monatomic system interacting via the Dzugutov pair potential, freezing of the fluid into an equilibrium dodecagonal quasicrystal has been reported [M. Dzugutov, Phys. Rev. Lett. **70**, 2924 (1993)]. Here, using a combination of molecular dynamics simulation and thermodynamic perturbation theory, we conduct a detailed analysis of the relative stabilities of solid-phase structures of the Dzugutov-potential system. At low pressures, the most stable structure is found to be a bcc crystal, which gives way at higher pressures to an fcc crystal. Although a dodecagonal quasicrystal and a  $\sigma$ -phase crystal compete with the bcc crystal for stability, they remain always metastable.

PACS numbers: 61.43.Bn, 61.44.Br, 61.50.Ah, 64.70.Dv, 64.70.Pf

## I. INTRODUCTION

Several years ago [1], Dzugutov introduced a new model pair potential for the purpose of studying glass transitions by means of molecular dynamics (MD) simulation. Most simulations of glass transitions to date have been performed using binary mixtures, since one-component simple liquids, when supercooled, readily nucleate crystallites. The Dzugutov potential, which features a pronounced maximum at a range typical of next-nearest-neighbor coordination distances in close-packed crystals, suppresses crystallization by construction, and thus facilitates glass formation. Following its initial successful use in studies of supercooled liquids [1,2], the Dzugutov potential was subsequently adopted in simulations of freezing [3,4]. Contrary to expectations, however, the observed solid structure was determined to be, remarkably, a monatomic dodecagonal quasicrystal. The structure, also known as tetrahedrally or topologically close packed (tcp) [5], is of the Frank-Kasper type and is composed of layers of square-triangle tilings. In previous work, the Dzugutov potential and the associated dodecagonal structure have been used to study self-diffusion in quasicrystals [6].

The motivation for the present work stems primarily from our interest in the nucleation and stability of quasicrystal phases. Further motivation comes from the realm of colloid physics, where, given the extreme tunability of colloidal interparticle interactions, it is conceivable that a Dzugutov-like pair potential might be engineered to produce bulk samples of one-component quasicrystals [7]. The main purpose of the study reported here is to chart, by means of both MD simulation and thermodynamic perturbation theory, the fluid-solid phase diagram of the Dzugutov-potential system.

The paper is organized as follows. In Section II, after specifying the pair potential, we give details of the simulation methods, and describe our analyses of the resulting solid structures. Section III outlines the theoretical methods used, while Section IV characterizes the quasicrystal and other structures of interest. In Section V we present results – from both simulation and theory – for relative stabilities of competing solid structures. Among our

main results, we find that (1) at low temperatures and pressures, the stable solid structure is the bcc crystal; (2) at high pressures, the stable solid is the fcc crystal; and (3) the stable ground state ( $T = 0$ ) is never the dodecagonal quasicrystal, but rather a periodic crystal whose structure depends on the pressure. Finally, in Section VI we summarize and discuss implications of the results for future work.

## II. MOLECULAR DYNAMICS SIMULATIONS

### A. The Interaction

The Dzugutov pair potential [2], plotted in Fig. 1, is defined by

$$\Phi(r) = \Phi_1(r) + \Phi_2(r), \quad (1)$$

where

$$\Phi_1(r) = \begin{cases} A(r^{-m} - B) \exp\left(\frac{c}{r-a}\right), & r < a \\ 0, & r \geq a, \end{cases} \quad (2)$$

and

$$\Phi_2(r) = \begin{cases} B \exp\left(\frac{d}{r-b}\right), & r < b \\ 0, & r \geq b, \end{cases} \quad (3)$$

with the parameters:

m	A	c	a	B	d	b
16	5.82	1.1	1.87	1.28	0.27	1.94

The potential is characterized by a minimum at  $r = 1.13 \sigma$  of depth  $-0.581 \epsilon$ , having the same form as that of the Lennard-Jones potential, followed by a maximum at  $r = 1.63 \sigma$  of height  $0.460 \epsilon$ . The maximum is designed to prevent the system from crystallizing into simple crystal structures. Beyond the maximum the potential tends to zero continuously and is cut off at a range of  $r_c = 1.94 \sigma$ , which ensures that CPU times remain within reasonable limits.

## B. Simulation Method

Classical isothermal (NVT) and isothermal-isobaric (NPT) MD simulations were performed using the constraint method [8]. An extension of this method allows us to introduce constant temperature or pressure gradients [9]. Newton's equations of motion were integrated using a fourth-order Gear predictor-corrector algorithm (see, *e.g.*, [8]) with a time increment of  $\delta t = 0.0005 \sigma \sqrt{m/\epsilon}$  for all simulations. Periodic boundary conditions were applied to an orthorhombic simulation cell, whose volume (in the NPT simulations) was permitted to change isotropically.

The sample sizes range from 54 to 1024 atoms, with the lengths of the cell along the three orthogonal coordinate axes being chosen to make the sample shapes as close to cubic as possible. Simulations with the stable phases were carried out with samples containing 54, 250, and 1024 atoms for bcc; 60 and 480 atoms for the  $\sigma$ -phase; and 108 and 500 atoms for fcc. Most results are reported for 250, 500, and 1024 atoms, though if not explicitly stated, the sample size is irrelevant. The potential energy and enthalpy per atom were found to be quite insensitive to sample size.

## C. Structural Analysis

To analyze the structures that arise in a simulation at finite temperature, we quenched the system by setting the temperature in our NPT-MD program to zero, thereby using the program as a steepest descent algorithm. Quenching forces the system to seek out its local energy minimum, which facilitates structure identification.

Dzugutov [2] has pointed out that vacancies may play a major role in stabilizing quasicrystalline structures. To determine the number of vacancies in a sample, we begin by constructing the Voronoi cells and their dual, the Delaunay cells, and determining from the latter the distribution of free volumes in the structure. Although the free volume distribution gives a reasonable representation of the interstitial sites, it greatly overestimates the

vacancies (by a factor of about ten). This is because the Delaunay cells are face-to-face packed tetrahedra, whereas the vacancies should be represented by spheres that could easily cover several tetrahedra. To determine the correct number of vacancies, we first select the Delaunay cells that are large enough to accommodate an atom and do not overlap with an already existing atom. With these cells we create trees of mutually overlapping cells, the nodes of the tree being the centers of the Delaunay cells and the edges the distance vectors between cells too close to be filled simultaneously. We then fill the tree with spheres, starting at the outermost ends. After adding a sphere, all the Delaunay cells connected to its node are discarded. The next sphere is then added onto the next outermost node remaining. The procedure is repeated until the whole tree is filled, after which the algorithm repeats with another Delaunay cell not belonging to the current tree. This method allows us to fill the sample as densely as possible with vacancies.

In order to help characterize and distinguish the solid structures observed in the simulations, we have computed from the atomic coordinates both radial and angular distribution functions. However, such averaged functions often do not allow unique identification of a structure, which requires as well the spatial distribution of bonds. Thus, we have also generated bond order diagrams. These are stereographic projections of the nearest-neighbor bonds constructed as follows. First, all neighbor vectors are determined and normalized to unit length. Next, the vectors are placed at a common origin so that their endpoints lie on the unit sphere. Finally, the distribution of the points on the sphere is represented by stereographic projections along the three coordinate axes. The pictures thus obtained reveal the global symmetry of the sample.

### III. THEORY

For comparison with the simulation data, we have independently calculated the phase behavior of the system by means of thermodynamic perturbation theory. Taking the Dzugutov pair potential as input, we apply the approximate theory of Weeks, Chandler, and Andersen

(WCA) [10] to a classical system of  $N$  pair-wise-interacting particles in a volume  $V$ . The WCA approach is especially well suited to pair potentials that contain a steeply repulsive core and has been successfully applied to the Lennard-Jones potential [11–13], which has a repulsive core similar to that of the Dzugutov potential.

The WCA approximation splits the pair potential  $\phi(r)$  at its first minimum into a short-range repulsive reference potential  $\phi_0(r)$  and a perturbation potential  $\phi_p(r)$  and prescribes a mapping of the reference system onto an effective hard-sphere (HS) system. The Helmholtz free energy  $F$  of the system separates correspondingly into reference and perturbation parts, according to

$$F = F_0 + \int_0^1 d\lambda \langle \Phi_p \rangle_\lambda, \quad (4)$$

where  $F_0$  is the free energy of the reference system,

$$\Phi_p \equiv \sum_{i < j} \phi_p(|\mathbf{r}_i - \mathbf{r}_j|) \quad (5)$$

is the total perturbation energy, and  $\langle \cdots \rangle_\lambda$  denotes averaging with respect to the probability distribution of a system with pair potential  $\phi_\lambda(r) = \phi_0(r) + \lambda\phi_p(r)$ . Expansion of  $\langle \Phi_p \rangle_\lambda$  in powers of  $\lambda$  about the reference system ( $\lambda = 0$ ) generates an exact perturbation series. Mapping the reference system onto an effective HS system, the free energy may be expressed, to *first-order* in the perturbation potential, as

$$F[\rho(\mathbf{r})] = F_{\text{HS}}[\rho(\mathbf{r})] + \frac{2\pi N^2}{V} \int_0^\infty dr' r'^2 g_{\text{HS}}(r'; [\rho(\mathbf{r})]) \phi_p(r'), \quad (6)$$

where  $F_{\text{HS}}[\rho(\mathbf{r})]$  and  $g_{\text{HS}}(r; [\rho(\mathbf{r})])$  are the free energy and radial distribution function (rdf), respectively, of the HS reference system, both functionals of the equilibrium one-particle number density  $\rho(\mathbf{r})$ . The rdf is defined, in turn, according to

$$g_{\text{HS}}(r; [\rho(\mathbf{r})]) \equiv \frac{1}{4\pi\rho^2 V} \int d\Omega \int d\mathbf{r}' \rho^{(2)}(\mathbf{r}', \mathbf{r}' + \mathbf{r}), \quad (7)$$

as an orientational and translational average of the two-particle density  $\rho^{(2)}(\mathbf{r}, \mathbf{r}')$ . The second- and higher-order terms are proportional to successively higher powers of inverse

temperature  $1/T$ , the coefficients being related to mean fluctuations of  $\Phi_p$  [14]. Accuracy of the first-order approximation [Eq. (6)] is thus assured as long as fluctuations in  $\Phi_p$  remain sufficiently small relative to the thermal energy  $k_B T$ .

The free energy of the fluid phase is calculated via the uniform limit ( $\rho(\mathbf{r}) \longrightarrow \rho$ ) of Eq. (6), using the essentially exact Carnahan-Starling and Verlet-Weis forms [14] for the HS free energy per particle,  $f_{\text{HS}}(\rho)$ , and rdf,  $g_{\text{HS}}(r)$ , respectively. For the solid phase, the HS free energy functional is approximated by means of classical density-functional (DF) theory [15]. The DF approach is based on the existence of a functional  $\mathcal{F}[\rho(\mathbf{r})]$  of the density  $\rho(\mathbf{r})$  that satisfies a variational principle, according to which  $\mathcal{F}[\rho(\mathbf{r})]$  is minimized – for given average density and external potential – by the equilibrium density, its minimum value equaling the Helmholtz free energy  $F$ . In the absence of an external potential,  $\mathcal{F}[\rho(\mathbf{r})]$  may be decomposed into an exactly known ideal-gas contribution

$$\mathcal{F}_{\text{id}}[\rho(\mathbf{r})] = k_B T \int d\mathbf{r} \rho(\mathbf{r}) [\ln(\rho(\mathbf{r}) \Lambda^3) - 1], \quad (8)$$

which is the free energy in the absence of interactions ( $\Lambda$  being the thermal de Broglie wavelength) and an excess contribution  $\mathcal{F}_{\text{ex}}[\rho(\mathbf{r})]$ , depending entirely upon internal interactions.

Here we approximate the excess free energy of the HS solid by the modified weighted-density approximation (MWDA) [16,17], which gives a reasonable description of the HS system. The MWDA maps the excess free energy per particle of the solid onto that of a corresponding uniform fluid of effective density, according to

$$\frac{1}{N} \mathcal{F}_{\text{ex}}^{\text{MWDA}}[\rho(\mathbf{r})] = f_{\text{HS}}(\hat{\rho}), \quad (9)$$

where the effective (or weighted) density

$$\hat{\rho} \equiv \frac{1}{N} \int d\mathbf{r} \int d\mathbf{r}' \rho(\mathbf{r}) \rho(\mathbf{r}') w(|\mathbf{r} - \mathbf{r}'|; \hat{\rho}) \quad (10)$$

is a self-consistently determined weighted average of  $\rho(\mathbf{r})$ . The weight function  $w(r)$  is specified by normalization and by the requirement that  $\mathcal{F}_{\text{ex}}^{\text{MWDA}}[\rho(\mathbf{r})]$  generate the exact two-particle (Ornstein-Zernike) direct correlation function  $c(r)$  in the uniform limit. This

leads to an analytic relation [16] between  $w(r)$  and the fluid functions  $f_{\text{HS}}$  and  $c(r)$ , computed here using the solution of the Percus-Yevick (PY) integral equation for hard spheres [14].

Practical calculation of  $F_{\text{HS}}[\rho(\mathbf{r})]$  and  $g_{\text{HS}}(r; [\rho(\mathbf{r})])$  requires specifying the solid density, *i.e.*, the coordinates of the lattice sites (equilibrium particle positions) and the shape of the density distribution about these sites. Here we consider fcc, hcp, bcc, and  $\sigma$ -phase crystals and the dodecagonal quasicrystal structures described below in Sec. IV. The density distribution is modelled by the Gaussian ansatz. This places at each site  $\mathbf{R}$  a normalized isotropic Gaussian, such that

$$\rho(\mathbf{r}) = \left(\frac{\alpha}{\pi}\right)^{3/2} \sum_{\mathbf{R}} \exp(-\alpha|\mathbf{r} - \mathbf{R}|^2), \quad (11)$$

the single parameter  $\alpha$  determining the width of the distribution. The Gaussian ansatz has been shown by simulation [18] to reasonably describe the density distribution of close-packed crystals. For nonoverlapping neighboring Gaussians – consistently the case here – the ideal-gas free energy per particle [Eq. (8)] is very accurately approximated by

$$\frac{1}{N} \mathcal{F}_{\text{id}} = \frac{3}{2} k_{\text{B}} T \ln(\alpha \Lambda^2) - \frac{5}{2}, \quad (12)$$

to within an irrelevant constant. The HS free energy is obtained, for a given solid structure and average density, by minimizing the approximate functional  $\mathcal{F}_{\text{HS}}[\rho(\mathbf{r})] = \mathcal{F}_{\text{id}}[\rho(\mathbf{r})] + \mathcal{F}_{\text{ex}}^{MWDA}[\rho(\mathbf{r})]$  [from Eqs. (9), (10), and (12)] with respect to  $\alpha$ . Predictions of the MWDA for free energies and pressures of HS solids are in good agreement with simulation data for both fcc [16] and bcc [19] crystals. Although the theory underpredicts, by roughly 20 %, the Lindemann ratios (ratio of root-mean-square particle displacement to nearest-neighbor distance) at melting for both crystal symmetries, it is only the free energies that determine thermodynamic phase behavior. Note that in simulations of the HS bcc crystal a constraint of single-cell occupancy is usually imposed in order to stabilize the crystal against shear.

The perturbation free energy in Eq. (6) requires knowledge of the hard-sphere rdf, which may be expressed, in general, as a sum over coordination shells:

$$g_{\text{HS}}(r; [\rho(\mathbf{r})]) = \sum_{i=1}^{\infty} g^{(i)}(r; [\rho(\mathbf{r})]). \quad (13)$$



The functionals  $g^{(i)}(r; [\rho(\mathbf{r})])$  are obtained using the approach of Rascón *et al.* [13], which approximates the second and higher coordination shells in mean-field fashion and corrects the first coordination shell for nearest-neighbor correlations. Thus, ignoring correlations for  $i \geq 2$ , and substituting  $\rho^{(2)}(\mathbf{r}, \mathbf{r}') = \rho(\mathbf{r})\rho(\mathbf{r}')$ , together with Eq. (11), into Eq. (7), yields

$$g^{(i)}(r; [\rho]) = \frac{1}{4\pi\rho} \left(\frac{\alpha}{2\pi}\right)^{1/2} \frac{n_i}{rR_i} \exp[-\alpha(r - R_i)^2/2], \quad i \geq 2, \quad (14)$$

where  $n_i$  is the coordination number and  $R_i$  the lattice vector magnitude of the  $i$ th shell. The first peak is parametrized by

$$g^{(1)}(r; [\rho(\mathbf{r})]) = \frac{A \exp[-\alpha_1(r - r_1)^2/2]}{r}, \quad r \geq d, \quad (15)$$

where  $d$  is the effective HS diameter and where the parameters  $A$ ,  $\alpha_1$ , and  $r_1$  are determined by imposing three sum rules, namely the virial equation (relating the contact value to the bulk pressure  $P$ ), normalization to the nearest-neighbor coordination number  $n_1$ , and approximation of the first moment by its mean-field value. Together then, the HS pressure  $P = \rho^2 \partial f_{\text{HS}} / \partial \rho$  and the value of  $\alpha$  that minimizes  $F_{\text{HS}}[\rho(\mathbf{r})]$  determine  $g_{\text{HS}}(r; [\rho(\mathbf{r})])$  and so the perturbation free energy for a given solid structure. The approximation expressed by Eqs. (13)-(15) is in excellent agreement with simulation data for the HS fcc crystal, and has been successfully applied, in a perturbation theory, to Lennard-Jones and square-well solids [13]. The approximation also has been tested against, and found to closely match, Monte Carlo simulation data for  $g_{\text{HS}}(r; [\rho(\mathbf{r})])$  of a HS bcc crystal (at density  $\rho\sigma^3 = 1.1$ ), subjected to a single-cell occupancy constraint to suppress shear instability [20]. Further simulations will be required, however, to test the approximation for the HS bcc crystal at lower densities, where next-nearest-neighbor correlations and anisotropies in the density distribution may not be negligible.

It remains still to specify the effective HS diameter  $d$ . According to the WCA prescription,  $d$  is the root of the nonlinear equation

$$\int d\mathbf{r} g_{\text{HS}}(r; [\rho(\mathbf{r})]; d) \Delta\epsilon(r) = 0, \quad (16)$$

where  $y_{\text{HS}}(r; [\rho(\mathbf{r})]; d) \equiv \exp[\phi_{\text{HS}}(r; d)/k_{\text{B}}T]g_{\text{HS}}(r; [\rho(\mathbf{r})]; d)$  is the HS cavity function and

$$\Delta e(r) = \exp[-\phi_0(r)/k_{\text{B}}T] - \exp[-\phi_{\text{HS}}(r; d)/k_{\text{B}}T] \quad (17)$$

is a function that is nonzero only over a narrow range  $\xi d$  ( $\xi \ll 1$ ) around  $r = d$ . This choice ensures that the free energy of the reference system differs from that of the effective HS system only by terms of  $O(\xi^4)$  and higher. In practice, lacking knowledge of the cavity function of the HS solid for  $r < d$ , we expand the quantity  $r^2 y_{\text{HS}}(r; [\rho(\mathbf{r})]; d)$  in a Taylor series about  $r = d$  and retain the first three terms.

The theory set out above provides a reasonable approximation for the Helmholtz free energy of the system at temperatures of order  $\epsilon/k_{\text{B}}$  and higher. From the free energy, any bulk thermodynamic property then may be calculated. Of particular relevance to phase behavior are the pressure and chemical potential. In Sec. V D, we present our theoretical predictions for the phase diagram of the Dzugutov-potential system.

## IV. SOLID STRUCTURES

### A. Dodecagonal Quasicrystal

The structural model of the dodecagonal quasicrystal that we have investigated is a layered system that is periodic in one direction, but quasiperiodic and twelve-fold symmetric in the perpendicular plane [21]. It is of Frank-Kasper type, *i.e.*, it is mostly tetrahedrally close-packed, and can be described as a periodic  $ABA\bar{B}$  stacking of a primary dodecagonal layer  $A$  and two secondary hexagonal layers,  $B$  and  $\bar{B}$ , which are rotated by  $30^\circ$  with respect to each other to obtain dodecagonal symmetry. The atoms in layer  $A$  form the vertices of a simple tiling made of squares, triangles,  $30^\circ$  rhombi and two kinds of hexagons. The threefold symmetric hexagon is known as the “shield”. These tiles, together with their decorations, are shown in Fig. 2. A sample of a square-triangle configuration is displayed in Fig. 3. The dodecagonal quasicrystal structure also can be regarded as the decoration of a simple dodecagonal tiling [22,23].

The stability of the monatomic Frank-Kasper-type decoration of the square-triangle-rhombi-shield tiling with the potential of Eq. (1) was reported by Dzugutov [3]. Upon cooling below the glass transition temperature, a glass forms, which transforms, after a very long annealing time, into a dodecagonal quasicrystal. The underlying tiling structure is mainly a decorated square-triangle tiling with a few rhombi and shields.

The aperiodicity of quasicrystals forbids periodic boundary conditions in the simulation. Taking a finite patch with open boundary conditions also should be avoided, as the surface energy would affect structural stability. A solution is to use periodic approximants, which are finite, orthorhombic cells whose boundaries match on opposite sides. In this way, periodic boundary conditions may be applied, as is done throughout this paper.

## B. Square-Triangle Crystals

In addition to the quasicrystalline tilings, it is also possible to generate crystalline phases with squares and triangles decorated in the same fashion as for the quasicrystals. If only squares are used, the A15- or  $\beta$ -W-phase (also known as cP8 Cr<sub>3</sub>Si) is obtained, whereas a pure triangle tiling results in the Z structure (hp7 Zr<sub>3</sub>Al<sub>4</sub>). If both squares and triangles are permitted, the  $\sigma$ -phase or  $\beta$ -U (also known as tp30 Cr<sub>46</sub>Fe<sub>54</sub>) and the H-phase are obtained. The two phases differ in the arrangement of the tiles. The vertex configurations of the crystalline phases are shown in Fig. 4. They are denoted by a, z, h,  $\sigma$  according to the phase in which they appear.

The unit cell of the  $\sigma$ -phase can be subdivided into two regular triangles and two squares. The atoms at the vertices of these tiles are 14-fold coordinated, while the atom in the center of the triangles is 15-fold coordinated. The remaining atoms on the edges and in the interior of the square are 12-fold coordinated icosahedra. Since all coordination shells have a triangular surface, all atoms are tetrahedrally close packed. Pure square-triangle structures and tilings with additional shields are very stable [21]. Rhombi, however, are unstable and transform into the other tiles.

## V. RESULTS

### A. Analysis and Comparison of Solid Structures

In this section we discuss the geometric properties of the amorphous structure, the bcc and fcc crystals, the nucleated tcp-phase, and the  $\sigma$ -phase. We have used three diagnostics to compare the structures: the radial distribution function (rdf), the angular distribution function (adf) of nearest neighbors separated by a distance less than the first minimum of the rdf (usually  $r < 1.6 \sigma$ ), and bond order diagrams, which aid in identifying the global symmetry even if the symmetry elements are oriented in random directions.

#### 1. Radial Distribution Functions

Figure 5a compares the radial distribution functions of the structures most commonly observed in the simulations. Typical of the amorphous structures is an asymmetric first peak, which appears to consist of two overlapping shells, followed by a second maximum in the range  $1.7 < r < 2.7 \sigma$ , which is the well-known double peak. The unusually sharp slope on the short-distance side indicates a well-defined second-nearest-neighbor distance, which is caused by the repulsive part of the maximum of the potential. The maximum at about  $1.9 \sigma$  is formed by two opposite corners of a bipyramid consisting of two regular tetrahedra. A second remarkable sharp slope is found at the third maximum at about  $2.7 \sigma$ . Notice that the rdfs of the tcp structures obtained on cooling are completely indistinguishable from the amorphous case.

The rdf of the  $\sigma$ -phase shows an example of the perfect square-triangle-rhombi-shield phases. The quasicrystalline and other crystalline and approximant phases differ only in the fine structure of the subpeaks. Evidently the tcp-phase rdf is a broadened envelope of the  $\sigma$ -phase rdf.

The rdfs of the bcc and fcc structures, however, are radically different. For bcc, the first maximum is indeed split, and in the second maximum the short-distance part is *lower*

than the next peak. This maximum is now formed by the distances across the tetragonal octahedron in the bcc structure. At higher temperatures, when the peaks of the rdf are broadened and overlap, the rdf of the bcc-phase is similar to the rdf of the tcp-phases except that the weights of the two subpeaks of the second maximum between  $1.7 \sigma$  and  $2.7 \sigma$  are interchanged.

The rdf of the fcc crystal exhibits a peak at about  $1.6 \sigma$ . Since this is the position of the potential maximum, it is clear that the fcc-phase is unstable at low pressures. Figure 5b shows the transition from a bcc-phase to the fcc-phase at  $k_B T/\epsilon = 0.75$ . The small maximum at  $1.5 \sigma$  indicates formation of regular squares, which are characteristic of fcc. The MD data are strikingly similar to theoretical predictions for the hard-sphere fcc crystal (Fig. 5c).

The sequence of phases at low temperatures and increasing pressure becomes clear when we examine the rdfs: for bcc and the  $\sigma$ -phase, the first two overlapping atomic shells occupy the minimum of the potential. The next shell is beyond the maximum. For fcc, the first shell is also in the minimum and the second shell is at the maximum. If the structures are compressed, the energies of bcc and the  $\sigma$ -phase *increase*, since the second maximum of the rdf moves up the maximum of the potential. The energy of fcc *decreases*, since the second maximum of the rdf moves down the potential maximum.

## 2. Angular Distribution Functions

The results for the angular distribution functions (Fig. 6) are consistent with the results for the rdfs. The amorphous and tcp structures are indistinguishable. The tcp-phase adf is a broadened version of the adf of the  $\sigma$ -phase. All of these phases, as well as the liquid show two maxima: a rather narrow extremum at small angles around  $60^\circ$  and a broad peak at about  $120^\circ$ . Both maxima indicate the existence of equilateral triangles. The adfs of bcc and fcc are again completely different. Especially remarkable are the maxima at an angle of  $90^\circ$ , indicating the existence of rectangles in these phases. For bcc these angles are formed

by distances between atoms along the four-fold axis.

### 3. Bond Order Diagrams

We have seen that the amorphous and tcp structures obtained by cooling cannot be distinguished by the rdf and adf. Are they really different? As shown in Fig. 7, bond order diagrams can give a clear answer. The diagram for bcc (Fig. 7a) is relatively simple, exhibiting seven maxima – four from the separation along the space diagonals and three from the distances along the four-fold directions. As the sample shown here was not perfect, thin bridges join the maxima. The liquid (not shown) is characterized by an isotropic distribution of the bonds covering the whole sphere homogeneously. The diagram for the tcp-phase (Fig. 7b) is somewhat more complicated, featuring an equator with twelve maxima indicating the presence of a quasicrystal. Other prominent features are two further circles of maxima at higher latitudes and two peaks at the poles. For non-perfect samples the distribution of the maxima is distorted, and the symmetry may not be dodecagonal. Occasional ring-like arrangements of overlapping maxima surrounded by further maxima suggest twinning and multi-grain samples.

Comparing samples classified as amorphous or tcp-phases, we find that a continuous transition between the two may be possible. In Fig. 7b the maxima can be seen quite clearly. In other samples, however, the maxima are almost obscured by a rather homogeneous background noise. Quenching and annealing improves the diagrams only marginally. It is possible that some of the amorphous samples actually consist of a number of micro-grains. If in fact the case, this would mean that the amorphous and tcp-phases have the same *local* arrangement of atoms, although the amorphous sample did not succeed in ordering globally.

### 4. Real-Space Representation of the Structures

Real space pictures (snapshots) of the samples also help to distinguish the structures. In most cases, the bcc samples look quite defect-free, with only the vacancies visible. Sometimes

we find two differently oriented domains in the simulation box. Liquid samples obviously do not show any regularities. In the quenched amorphous structures, however, there are sometimes partially ordered parts, underlining our claim that they contain micrograins. The tcp samples, as exemplified by Fig. 7c, have layered structures, which, if viewed perpendicular to the layers, resemble the perfect sample in Fig. 3, characterized by centered ring-like structures formed by the 14- and 15-fold coordinated atoms. The quality of the pictures is often low, however, as the samples may be twinned or contain several grains.

## B. Ground-State Structures

The equilibrium structure of a specific potential at a given temperature and pressure may be determined, in principle, by a global minimization of the Gibbs free energy  $G$ . In practice, however, this procedure is not feasible with MD simulations, since direct transitions between local minima are rarely observed. Even if special methods are used to switch between closely related structures like bcc and fcc, there still may exist a free energy barrier high enough to prevent a transition [24]. Instead of attempting to minimize  $G$ , one identifies promising structures, computes the thermodynamic functions, and compares them. An alternative is thermodynamic integration of  $P$ , starting at  $P = 0$  and integrating towards higher pressures.

At  $T = 0$ , where entropy no longer affects stability, identifying the ground state simplifies considerably. Here the Helmholtz free energy  $F$  equals the internal energy  $U$ , which in turn equals the potential energy  $E_{\text{pot}}$ , since the kinetic energy vanishes. Furthermore, the Gibbs free energy  $G$  becomes equal to the enthalpy  $H$  and the pressure  $P$  is determined by the virial equation, since the kinetic pressure  $k_{\text{B}}T$  also vanishes. Common tangent constructions on curves of  $U(V, T = 0)$  vs.  $V$  yield the stability ranges of competing phases and curves of enthalpy  $H(P, T = 0)$  vs.  $P$  intersect at the phase coexistence pressures.

We have calculated the ground-state energies by two independent methods. First, taking the perfect structures, we have computed lattice summations of the Dzugutov pair potential. Second, starting from a perfect structure, we have relaxed the system with the MD simulation

program in an isothermal-isobaric ensemble, setting  $k_{\text{B}}T/\epsilon = 0.001$  and  $P$  to the desired value. In this mode, molecular dynamics acts as a steepest-gradient optimization algorithm. The pressure is derived from the virial equation. In contrast to a lattice sum calculation, where only the volume is scaled, in the simulations all atoms may move independently. Therefore the results may (and do) differ slightly from the lattice sum calculations for perfect structures.

Since the Dzugutov potential [Eq. (1)] is isotropic and has a single minimum, it should favor densely packed structures if the volume is not restricted. An optimal packing in three dimensions would consist of regular tetrahedra, but such a packing does not exist. Now there are two choices to solve this dilemma: either introduce other coordination polyhedra, as in fcc crystals, or use irregular tetrahedra, as in tcp phases. In the Frank-Kasper phases the coordination polyhedra are additionally restricted to deltahedra with five or six triangles meeting at a vertex. This condition is fulfilled for the icosahedron, and certain polyhedra with 14, 15 and 16 vertices. Although bcc is tetrahedrally close-packed, it is not a Frank-Kasper phase since its coordination polyhedron (a rhombic dodecahedron) has vertices where only four triangles meet.

In a first step towards identifying stable structures we study stacking variants, distort the phases mentioned above, and examine various tcp structures. The fcc structure can be modified by stacking the densely packed layers differently. We find that the hexagonal close-packed (hcp) and other stacking variants are considerably less stable than fcc at high pressures where fcc is more stable than bcc and the  $\sigma$ -phase. This result is remarkable since for the Lennard-Jones potential hcp is known to be slightly more stable than fcc [25].

Distortions of the bcc phase along the principal symmetry axis always reduce the stability. The same happens for the  $\sigma$ -phase if the layer distance is changed from the optimum at  $c/a = 1.03$  ( $a$  is the edge length of the tiles and  $c$  the period along the  $z$ -axis).

The Frank-Kasper phases are of two types: structures with 16-fold coordinated sites and structures without. The dodecagonal quasicrystal, its approximants, and crystalline variants are of the latter type, called the square-triangle class. Structures containing 16-fold



(or higher) coordinated atoms have a lower stability. The sites with the high coordination numbers are too numerous and the potential energy increases because of strained bonds.

We observe the same trend in the square-triangle class. The stability is lowest for the purely triangular Z-phase since the number of 15-fold sites is also considerable. The stability increases if the triangles are separated by squares, but is again rather low if the structure contains only squares as in the A-phase without 15-fold sites, perhaps because the A-phase has full cubic symmetry and is therefore more rigid than the other structures. The  $\sigma$ -phase, on the other hand, is more stable than the H-phase, since it contains only pairs of triangles instead of rows. More complicated crystalline phases, approximants, and the quasicrystals all contain mixtures of squares and triangles in different arrangements. These structures are all inferior to the  $\sigma$ -phase since they must contain larger conglomerates of triangles.

In a second step towards identifying ground-state structures, we survey the published crystallographic structures. From the lists in Refs. [26–28], a variety of structures have been selected according to the following criteria:

1. Coordination numbers between 10 and 15.
2. Derivatives of tcp structures.
3. Derivatives of bcc, especially vacancy-ordered structures.
4. Quasicrystal approximants.
5. Icosahedral coordination shells.

For each structure examined the required crystallographic data were taken from Ref. [5]. A full list of the structures is given in the Appendix.

Assembling the results, the following picture emerges at  $T = 0$  (Fig. 8): the bcc-phase has the absolute minimum potential energy at a density of  $\rho\sigma^3 = 0.866$ . The  $\sigma$ -phase acts as the lower bound for all the square-triangle phases, being minimal at  $\rho\sigma^3 = 0.879$ . The fcc-phase has a potential energy minimum at  $\rho\sigma^3 = 1.013$ . A common tangent construction shows that

bcc is stable up to  $\rho\sigma^3 = 0.887$ , and fcc is stable above  $\rho\sigma^3 = 1.057$ . The relaxed  $\sigma$ -phase is stable, as determined by MD, only within the narrow interval  $0.887 < \rho\sigma^3 < 1.057$ , whereas the ideal  $\sigma$ -phase is never stable, according to a simple lattice sum calculation. Intersections of the enthalpy curves yield the stability ranges in terms of pressure. The most stable structures are bcc for  $P\sigma^3/\epsilon < 1.70$ ,  $\sigma$  for  $1.70 < P\sigma^3/\epsilon < 2.85$ , and fcc for  $P\sigma^3/\epsilon > 2.85$ . The sequence of ground-state structures with increasing pressure (and density) is therefore: bcc –  $\sigma$  – fcc. The properties of the various structures are summarized in Table I.

Vacancy-ordered phases are more stable than pure bcc at densities down to  $\rho\sigma^3 = 0.7$  (Fig. 8b). In the range  $0.6 < \rho\sigma^3 < 0.7$  the lowest potential energy is attained by a disordered phase formed upon annealing the NiTi<sub>2</sub> approximant phase.

### C. Finite-Temperature Phases

From the ground-state calculations we have determined the stable structures at  $T = 0$ . Insight into the topology of the phase diagram at finite temperatures now can be obtained by observing phase transitions between the melt and the solid upon heating, cooling, and compression. As noted in Sec. V B, it is not possible to determine the relative thermodynamic stabilities of two competing phases directly from conventional MD simulations because of the difficulty of computing the entropic contribution to the free energy. However, by observing the temperature and pressure at which a phase becomes unstable, it is possible to establish limits of mechanical stability. The results of our MD stability analysis are consolidated in Fig. 10a.

#### 1. Heating Simulations

If the bcc and  $\sigma$ -phase solids are heated at low pressure, the energy and enthalpy for bcc remain always lower than those for the  $\sigma$ -phase. At higher pressures, the energy of the  $\sigma$ -phase drops below that of bcc. The differences between the enthalpies at higher

temperatures, however, are smaller than their fluctuations, such that the relative stabilities of bcc and the  $\sigma$ -phase cannot be resolved.

The determination of the melting line has been discussed in detail in Ref. [29]. Here we present only a brief summary. The phase transition line was determined by preparing a solid at  $k_B T/\epsilon = 0$  or 0.4 at fixed pressure and heating it continuously at rates of  $k_B \delta T/\epsilon = 0.001$  or 0.002 per timestep until melting was observed. The criterion for melting was the divergence of the mean-square displacement. At the same temperature a sudden rise in the potential energy and an associated drop in the density were observed. Similar simulations have been carried out at constant volume starting at  $k_B T/\epsilon = 0.001$  and  $P\sigma^3/\epsilon = 0.001$ . We emphasize that the transition line thus obtained is not strictly the equilibrium melting line, since with periodic boundary conditions the sample has no surface at which melting could start and a two-phase coexistence is not possible because the samples are too small. The solid-fluid transition lines differ only slightly for bcc and the  $\sigma$ -phase. The fcc crystal melts at somewhat higher temperatures. At high pressures, however, the  $\sigma$ -phase becomes unstable at considerably lower temperatures than bcc and fcc.

The transition to the fluid also can be determined by expanding a solid at constant temperature starting from high densities. The transition line obtained in this way for bcc crystals is the same as that determined by heating within the statistical fluctuations (Fig. 10a). As noted in Ref. [29], only one fluid phase is observed and no transition between a liquid and a vapor phase could be found.

## 2. Cooling Simulations

Cooling simulations were carried out in a manner similar to the heating runs. Starting samples were obtained from solids equilibrated at high temperatures. The cooling rate was  $k_B \delta T/\epsilon = 0.002$  per time step. Similar to melting, the freezing transition is delayed, now because critical nuclei first must be formed, and subsequent large-scale reordering of atoms may be necessary.

We find that the phase nucleating at pressures above  $P\sigma^3/\epsilon = 5$  always has bcc symmetry. If the temperature is lowered to about  $k_B T/\epsilon = 0.7 - 1.0$ , bcc becomes unstable relative to fcc at pressures above  $P\sigma^3/\epsilon = 20$ . Although a complete transition to fcc cannot be achieved with our simulation method, we observe a clear indication that fcc is the preferred structure. In the radial distribution function (Fig. 5a) we observe the emergence and growth of a new peak between the first and the second peaks at about  $\sqrt{2}$  times the nearest-neighbor distance, which signals the formation of regular squares in the close-packed crystal structures.

Below  $P\sigma^3/\epsilon = 5$  we do not observe a typical freezing transition with a jump in potential energy, but only a sharp kink, reminiscent of a glass transition. The nucleating structures are partially ordered and possess features typical of the tcp structure, namely layering, ring-like structures, and the Frank-Kasper polyhedra (see Fig. 7c). In the following, we refer to such structures as the tcp-phase. Although sometimes dodecagonal, the tcp structures often do not have a perfect symmetry, and thus may have varying degrees of crystallinity.

Because of the maximum in the potential, it was not possible in general to obtain perfect samples. If the pressure is too low, there is insufficient cohesion to compactify the samples. This is clearly seen by comparing runs with different cooling rates. However, if equilibrated for a longer time, the samples eventually become much denser.

The density ranges for stability have been obtained by cooling at constant volume. For the 500-atom sample we obtain the boundary between the formation of the bcc and the tcp-phase at  $\rho\sigma^3 = 0.87$ , independent of the cooling rate up to  $k_B\delta T/\epsilon = 0.0005$  per time step. For the 1024-atom sample, however, the boundary is shifted to  $\rho\sigma^3 = 0.84$  and is observed at the first time for  $k_B\delta T/\epsilon = 0.00025$  per time step. This is remarkable, since the minimum of the  $\sigma$ -phase lies at about  $\rho\sigma^3 = 0.9$ .

The formation of the crystalline structures also depends on the sample sizes and the cooling rates. A sample with 250 atoms and a constant density of  $\rho\sigma^3 = 0.865$  froze to bcc at a cooling rate of  $k_B\delta T/\epsilon = 0.001$ . For 500 atoms we had to reduce the cooling rate by a factor of one half, and for 1024 atoms a cooling rate of  $k_B\delta T/\epsilon = 0.00025$  per time step was necessary to obtain a perfect bcc phase, although partial bcc ordering was already observed

at twice this rate.

It is easier to obtain the tcp-phase in a constant volume simulation (as Dzugutov did) rather than in a constant pressure ensemble. To some extent, the nucleated structures can be annealed also at constant volume. However, most of the defects, especially different domains, cannot be so removed. Annealing at constant pressure also turns out to be ineffectual.

The transition from fluid to solid also may be observed by compressing the fluid at a constant pressure gradient of  $\delta P \sigma^3 / \epsilon = \pm 0.1$ . The transition curve is the same as for cooling (Fig. 10a), the collapsed structures being again bcc, at least for  $k_B T / \epsilon = 0.6, 0.8, 1.0, 1.5$ , and 2.5.

Between the melting and freezing curves we observe a broad hysteresis region, within which the thermodynamic phase transition should occur. The reason for the broad hysteresis region is the peculiar form of the potential. The maximum strongly inhibits freezing and collapsing of the structure, indeed as intended by Dzugutov [30].

The structures generated by cooling the samples contain free volumes even if the density or pressure during nucleation is high. In the case of constant volume cooling the reason is obvious, since the volume of the nucleating regions shrinks with temperature. However, constant pressure cooling also generates free volumes, even at high pressures, since at the onset of nucleation the frozen domains have a higher density than the liquid. The rigidity of the solid prevents the simulation box from contracting fast enough. With the methods described in Sec. II C, we can show that the free volumes in the ordered phases are mostly vacancies.

If the simulation samples are quenched to  $T = 0$  and  $P = 0$ , and the vacancies are filled with atoms, we find that the density of bcc rises to  $\rho \sigma^3 = 0.864 \pm 0.005$ , whereas the densities of the tcp-phase remain at about  $\rho \sigma^3 = 0.847 \pm 0.005$ . Although the densities of the bcc samples are close to the ideal value of 0.8638, the densities of the tcp-phase are far lower than the ideal value at the potential energy minimum ( $\rho \sigma^3 = 0.881$ ).

### *3. Compression Simulations*

If the structures are compressed at fixed temperature, bcc destabilizes first. One might therefore expect bcc to be stable only at relatively low temperatures. However, this would contradict the cooling simulations (Sec. V C 2), which yield a bcc structure. A full picture can be obtained only by calculating the Gibbs free energy, since it may be kinetically favorable for the system to nucleate bcc crystallites.

At high pressures the stable structure is clearly fcc, which has the lowest energy and enthalpy. Upon compression, this close-packed structure remains stable, and radial distribution functions of the decaying bcc and  $\sigma$ -phase structures show new peaks characteristic of fcc.

## **D. Theoretical Predictions**

For comparison with the MD simulation data, we have applied the perturbation theory described in Sec. III to predict the thermodynamic phase behavior of the Dzugutov-potential system. For the fluid phase and selected solid structures, free energies were calculated and a coexistence analysis performed. Our choice of structures was dictated by the structures actually observed in the simulations. Figure 9 compares the HS part of the free energy for the fcc, bcc, and  $\sigma$ -phase structures. Also shown, for comparison, are corresponding Monte Carlo simulation data from Ref. [19]. From the maximum HS volume fractions of these structures – respectively 0.74, 0.68, and 0.53 – stability of the HS solid is seen to be strongly influenced by packing efficiency. Therefore, at high temperatures and pressures, where entropy dominates the free energy and the system behaves as an effective HS system, the structures that are more efficiently packed are favored. As temperature and pressure decrease, internal energy makes an increasing contribution to the free energy. As illustrated by the neighbor distance histograms (Fig. 1) and the corresponding hard-sphere rdfs (Fig. 5c), the first few coordination shells of the bcc and  $\sigma$ -phase structures are more commensurate with the

attractive part of the Dzugutov potential than those of the fcc crystal, favoring these more loosely packed structures over close-packed fcc.

Constructing Maxwell common tangents to curves of free energy per volume vs. density, thus ensuring equality of chemical potentials and pressures in coexisting phases, we have mapped out the phase diagram of the system. Projections onto the  $P - T$  and  $T - \rho$  planes are shown in Figs. 10b and 11, respectively. As anticipated, the stable solid at high pressures is the fcc crystal, while the bcc crystal is only metastable relative to fcc (long-dashed curve in Fig. 10b). Aside from fcc, bcc, and  $\sigma$ -phase, we have also considered several tcp structures observed in the simulations and rational approximants to layered dodecagonal quasicrystals. The tcp and quasicrystal structures, however, were found to be at best only metastable relative to the crystal structures. At  $T = 0$ , lattice-sum calculations of ground-state energies (Fig. 8a) show that bcc is the stable structure for  $P\sigma^3/\epsilon < 2.66$ . From this known limit, we postulate that bcc is also the stable solid structure at low  $P$  for small but finite temperatures. The perturbation theory being of uncertain accuracy for  $k_B T/\epsilon < 0.5$ , we further postulate an extrapolation of the fluid-fcc phase boundary to zero pressure. This confines the stable bcc phase to a small pocket in the lower-left corner of the  $P - T$  diagram.

## VI. DISCUSSION AND CONCLUSIONS

The pressure-temperature phase diagram of the Dzugutov potential obtained by MD simulation is surprisingly rich. At low pressures and temperatures, the bcc-phase is stable, followed, with increasing pressure, by the  $\sigma$ -phase and by fcc (Fig. 10a). The bcc crystal is nucleated from the fluid for sufficiently slow cooling rates and sufficiently high density or pressure. It is also obtained by compressing the fluid. Below  $P\sigma^3/\epsilon = 5$  or  $\rho\sigma^3 = 0.85$ , tcp structures, including the dodecagonal quasicrystal, are formed. The cooling scenario may be summarized as follows:

1. At high cooling rates a glass is formed, which may be transformed into tcp or bcc solids by annealing at  $k_B T/\epsilon = 0.4 - 0.5$ .

2. At lower rates the fluid has sufficient time to reorder locally and crystallizes into a bcc crystal. The bcc structure being relatively simple, the samples are in most cases perfect except for vacancies.
3. At sufficiently low density or pressure, a tcp structure is generated. Characterized by layered symmetry, the tcp-phase can be formed for a wide variety of coordination polyhedra and many energetically similar configurations.
4. If the bcc crystal is cooled at high pressures or compressed at low temperatures, it transforms, at least partially, into the fcc structure.

The stability of the lowest energy tcp-phase, namely the  $\sigma$ -phase, relative to bcc, could not be determined precisely by our simulations. Heating at low pressure shows that the energy and enthalpy of bcc are always lower than those of the  $\sigma$ -phase. Comparing the two phases at higher pressures and temperatures shows that the difference in enthalpy is no longer significant, but the energy of the  $\sigma$ -phase becomes lower than that of bcc at higher pressures and temperatures. Furthermore, upon compression bcc becomes unstable at lower pressure than the  $\sigma$ -phase. The detailed topology of the phase diagram in Fig. 10a is still not completely clear and further simulations are necessary to compute the phase boundaries exactly. At low temperatures bcc appears at *lower* pressures than the  $\sigma$ -phase, whereas in the cooling simulations bcc is formed at *higher* pressures compared to the tcp structures. It may be, as speculated by Dzugutov [2], that entropy lowers the free energy of the  $\sigma$ -phase, and especially of the quasicrystal, thus leading to a stable tcp or quasicrystalline state at higher temperatures.

Our theoretical calculations for a selection of perfect solid structures suggest that the thermodynamically stable solid phases of the Dzugutov-potential system are limited to fcc and bcc crystals. Lattice-sum calculations at  $T = 0$  show that the  $\sigma$ -phase is almost degenerate with, though of slightly higher energy than, the bcc crystal. At high temperatures ( $k_B T \gg \epsilon$ ), where the attractive well in the potential plays only a minor role, packing efficiency strongly disfavors the  $\sigma$ -phase relative to both fcc and bcc crystals. At intermediate



temperatures ( $k_B T \simeq \epsilon$ ), perturbation theory predicts fcc and bcc crystals to be always more stable than the relatively loosely packed  $\sigma$ -phase. Thus the  $\sigma$ -phase appears nowhere in the  $P - T$  phase diagram and the bcc crystal appears only at low  $P$  and  $T$ .

It may be, of course, that the first-order perturbation theory lacks sufficient accuracy to conclusively resolve relative stabilities of such closely competing phases. In particular, fluctuations in the total perturbation energy, being stronger for a disorder fluid than for ordered solids, render the theory inherently less accurate for the fluid phase. Moreover, the mean-field neglect of next-nearest-neighbor correlations in the HS rdf is less justifiable for more open structures, such as bcc and the  $\sigma$ -phase, than it is for the close-packed fcc crystal. Such correlations, if significant, would tend to lower the free energies of the open structures and might possibly influence the order of stabilities.

Nevertheless, it should be emphasized that the predicted phase diagram is not necessarily at odds with the simulation data, if the tcp and high- $T$  bcc phases, observed in the simulations, are regarded as *metastable* with respect to fcc. Conceivably, for kinetic reasons, the supercooled fluid first nucleates a metastable bcc crystallite, which upon growth transforms into a stable fcc crystal. In fact, such behavior has been predicted from a general density-wave instability argument [31], and has been observed in simulations of a supercooled Lennard-Jones fluid [32]. Furthermore, whereas the theory has been applied to perfect structures, the simulations often result in solids replete with defects. We may conjecture, therefore, that the defects in the  $\sigma$ - and tcp-phases observed in the simulations serve to improve the packing efficiencies (*e.g.*, by increasing nearest-neighbor distances), while approximately preserving the average coordination distances, thereby conferring energetic advantage over the fcc structure.

After examining a wide variety of solid structures as candidates for stable phases of the Dzugutov potential, we are drawn to conclude that only such simple structures as bcc or fcc are competitive. A possible exception is the  $\sigma$ -phase, a tetrahedrally close-packed structure, although one of the simplest examples of its class. These results appear to place the Dzugutov potential in line with the Yukawa, generalized Lennard-Jones, Rubidium,

and Morse potentials, all of which favor bcc, fcc, or hcp crystals, supporting the general principle that simple pair potentials tend to favor simple structures. Nevertheless, it remains conceivable that quasicrystals and other complex structures, such as A15, Z, or H, might gain stability through modifications of the Dzugutov potential. Indeed previous work has identified somewhat related pair potentials for simple metals – albeit with no counterpart in the periodic table – for which stable icosahedral quasicrystals have been predicted [33,34]. Future work along these lines could examine variations of the Dzugutov potential in attempts to modify the relative stabilities of the tcp-phases and dodecagonal quasicrystals.

## ACKNOWLEDGMENTS

We thank H.-R. Trebin for a careful reading of the manuscript and Franz Gähler for supplying the data for the quasicrystal structures and some of the square-triangle crystal structures. ARD gratefully acknowledges the Forschungszentrum Jülich for use of its computing facilities.

## APPENDIX

The following lists contain the structures investigated as possible ground states in the MD simulations. The notation is as found in Ref. [5].

Stacking variants of fcc(abc): hcp(ab), abcacb, abcbcb.

Frank-Kasper phases: A15 or  $\beta$ -W (cP8 Cr<sub>3</sub>Si), Z (hp7 Zr<sub>3</sub>Al<sub>4</sub>),  $\sigma$ -phase or  $\beta$ -U (tP30 Cr<sub>46</sub>Fe<sub>54</sub>), H, J, F, K', C15 (cF24 MgCu<sub>2</sub>), T (cI162 Mg<sub>32</sub>(ZnAl)<sub>49</sub>),  $\mu$  (hR13 Fe<sub>7</sub>W<sub>6</sub>), D (V<sub>26</sub>Fe<sub>44</sub>Si<sub>30</sub>).

Square-triangle phases: A, H, Z,  $\sigma$ -phase, J, F, K', inflations of A and Z, doubling of the tiles of  $\sigma$ -phase, a phase with a and h sites mixed, tetragonal approximants of the quasicrystal with 23, 36, 172 and 836 tiles.

Vacancy ordered phases derived from bcc: cP1, cI10  $\beta$ -Hg<sub>4</sub>Pt, cF12 CaF<sub>2</sub>, tC14 AsPd<sub>5</sub>Tl, cI52 Cu<sub>5</sub>Zn<sub>8</sub>, cF120 Pd<sub>4-x</sub>Te, cF120 Sc<sub>11</sub>Ir<sub>4</sub>, cF116 Mn<sub>23</sub>Th<sub>6</sub>, cF88 Bi<sub>4</sub>Cu<sub>4</sub>Mn<sub>3</sub>, cI112

$\text{Ga}_4\text{Ni}_3$ .

The other structures are: oP12  $\text{Co}_2\text{Si}$ , oP16  $\text{AlDy}$ , oC8  $\text{BCr}$ , oC10  $\text{AlFe}_2\text{B}_2$ , oC12  $\text{Ge}_2\text{Th}$ , oC12  $\text{Si}_2\text{Zr}$ , oC16  $\text{BCMo}_2$ , oC16  $\text{Ga}_3\text{Pt}_5$ , oC16  $\text{HgNa}$ , oC28  $\text{Al}_6\text{Mn}$ , oI10  $\text{B}_2\text{CoW}_2$ , oI12  $\text{Gd}_2\text{Si}_3$ , oI16  $\text{BMo}$ , oI20  $\text{Al}_4\text{U}$ , oF24  $\text{Si}_2\text{Ti}$ , oF48  $\text{CuMg}_2$ , tp14  $\text{Hg}_5\text{Mn}_2$ , tP20  $\text{Al}_2\text{Gd}_3$ , tP30  $\text{AlNb}_2$ , tI12  $\text{Al}_2\text{Cu}$ , tI12  $\text{Si}_2\text{Th}$ , tI16  $\text{BMo}$ , tI28  $\text{MnU}_6$ , tI32  $\text{Si}_3\text{W}_5$ , hP3  $\text{Cd}_2\text{Ce}$ , hP3  $\text{AlB}_2$ , hP5  $\text{Al}_3\text{Ni}_2$ , hP6  $\text{InNi}_2$ , hP6  $\text{CaIn}_2$ , hR7  $\text{B}_5\text{Mo}_2$ , cP8  $\text{FeSi}$ , cP20  $\text{Mn}$ , cP39  $\text{Mg}_2\text{Zn}_{11}$ , cP138  $\text{Al}_9\text{Mn}_2\text{Si}_{11}$ , cP140  $(\text{AlSi})_{58}\text{Mn}_{12}$ , cI12  $\text{Ga}$ , cI26  $\text{Al}_{12}\text{W}$ , cI58  $\text{Mn}$ , cI76  $\text{Cu}_{15}\text{Si}_4$ , cF96  $\text{NiTi}_2$ .

## REFERENCES

- [1] M. Dzugutov and U. Dahlborg, J. Non-Crystalline Solids **131-133**, 62 (1991).
- [2] M. Dzugutov, Phys. Rev. A **46**, R2984 (1992).
- [3] M. Dzugutov, Phys. Rev. Lett. **70**, 2924 (1993).
- [4] The vibrational properties of the  $\sigma$  phase have been recently analysed: S. I. Simdyankin, S. N. Taraskin, M. Dzugutov, and S. R. Elliott, preprint (Los Alamos e-print archive, <http://xxx.lanl.gov/cond-mat/0002243>).
- [5] J. L. C. Daams, P. Villars, and J. H. N. van Vucht, *Atlas of Crystal Structure Types for Intermetallic Phases* (ASM International, Materials Park, 1991).
- [6] J. Roth and F. Gähler, Euro. Phys. J. B **6**, 425 (1998).
- [7] A. R. Denton and H. Löwen, Phys. Rev. Lett. **81**, 469 (1998).
- [8] M. P. Allen and D. J. Tildesley, *Computer Simulations of Liquids* (Oxford Science Publications, Oxford, 1987).
- [9] F. Lançon and L. Billard, J. Phys. France **49** 249 (1988).
- [10] J. D. Weeks, D. Chandler and H. C. Andersen, J. Chem. Phys. **54**, 5237 (1971).
- [11] W. A. Curtin and N. W. Ashcroft, Phys. Rev. A **32**, 2909 (1985).
- [12] L. Mederos, G. Navascués and P. Tarazona, Phys. Rev. E **49**, 2161 (1994).
- [13] C. Rascón, L. Mederos, and G. Navascués Phys. Rev. Lett. **77**, 2249 (1996).
- [14] J.-P. Hansen and I. R. McDonald, *Theory of Simple Liquids*, 2<sup>nd</sup> edition, (Academic Press, London, 1986).
- [15] D. W. Oxtoby, in *Liquids, Freezing, and Glass Transition*, Les Houches session 51, edited by J.-P. Hansen, D. Levesque, and J. Zinn-Justin (North-Holland, Amsterdam, 1991).

- [16] A. R. Denton and N. W. Ashcroft, Phys. Rev. A **39**, 4701 (1989).
- [17] W. A. Curtin and N. W. Ashcroft, Phys. Rev. Lett. **56**, 2775 (1986); **57** E1192 (1986).
- [18] R. Ohnesorge, H. Löwen H., and Wagner, Europhys. Lett. **22**, 245 (1993); D. A. Young and B. J. Alder, J. Chem. Phys. **60**, 1254 (1974).
- [19] W. A. Curtin and K. Runge, Phys. Rev. A **35**, 4755 (1987).
- [20] M. Watzlawek, private communication.
- [21] J. Roth and F. Gähler, in *Diffusion in Materials*, edited by H. Mehrer, Chr. Herzig, N.A. Stolwijk, H. Bracht, Defect and Diffusion Forum **143-147**, 815 (1997).
- [22] F. Gähler, in *Quasicrystalline Materials*, edited by Ch. Janot and J. M Dubois, p. 272 (World Scientific, Singapore, 1988).
- [23] C. Beeli, F. Gähler, H.-U. Nissen, and P. Stadelmann, J. Phys. France **51**, 661 (1990).
- [24] M. O. Robbins, K. Kremer, and G. S. Grest, J. Chem. Phys. **88**, 3286 (1988).
- [25] B. van den Waal, Phys. Rev. Lett. **67**, 23 (1991).
- [26] E. E. Ellner and R. Schwarz, in *Intermetallic Compounds*, Vol. 1: Principles, Chap. 13, edited by J. H. Westbrook and R. L. Fleischer, p. 309 (John Wiley, Chichester, 1994).
- [27] W. B. Pearson, *The Crystal Chemistry and Physics of Metals and Alloys* (Wiley-Interscience, New York, 1958).
- [28] P. Villars, K. Matthis, and F. Hullinger, in *Cohesion and Structure*, Vol. 2, Chap. 1, edited by F. R. de Boer and D. G. Pettifor (North Holland, Amsterdam, 1989).
- [29] J. Roth, Euro. Phys. J. B (accepted for publication).
- [30] For the Lennard-Jones potential our simulation methods work much better. Although it may not be possible to derive the melting line with high accuracy, there is no problem in observing all three phases and the transitions between them.

- [31] S. Alexander and J. P. McTague, Phys. Rev. Lett. **41**, 702 (1978).
- [32] P. R. ten Wolde, M. J. Ruiz-Montero, and D. Frenkel, Phys. Rev. Lett. **75**, 2714 (1995).
- [33] A. P. Smith, Phys. Rev. B **43**, 11635 (1991); Phys. Rev. B **42**, 1189 (1990); A. P. Smith and N. W. Ashcroft, Phys. Rev. B **38**, 12942 (1988).
- [34] A. R. Denton, J. Hafner, Phys. Rev. B **56**, 2469 (1997); Europhys. Lett. **38**, 189 (1997).

## TABLES

TABLE I. Ground-state structure and reduced density  $\rho\sigma^3$  at which the potential energy per atom  $E_{\text{pot}}$  is minimal. The upper half contains MD results at  $k_{\text{B}}T/\epsilon = 0.001$ , the lower half lattice sum calculations for perfect structures.

structure	$\rho\sigma^3$	U
fcc	1.013	-2.19
bcc	0.866	-2.66
$\sigma$	0.879	-2.57
fcc	1.057	-2.22
bcc	0.885	-2.29
$\sigma$	0.90	-2.27

## FIGURES

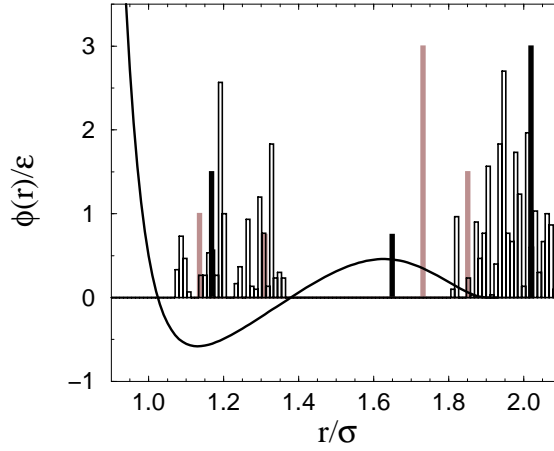


FIG. 1. Dzugutov pair potential together with histograms of neighbor distances for fcc (black bars), bcc (gray bars), and  $\sigma$ -phase (unshaded bars) crystals at reduced density  $\rho\sigma^3 = 0.9$ . Heights of bars are proportional to numbers of neighbors.

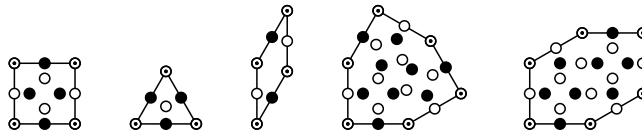


FIG. 2. The basic tiles of the dodecagonal model: square, triangle, rhombus, shield, twofold symmetric hexagon. The dotted atoms are placed in  $A$ -layers  $z = 1/4$  and  $3/4$ , the white atoms in  $B$ -layers at  $z = 0$  and the black atoms at  $Z = 1/2$ . All tiles can also occur with black and white atoms exchanged, depending on their orientation. The twofold symmetric hexagon is unstable and does not occur in our tilings.



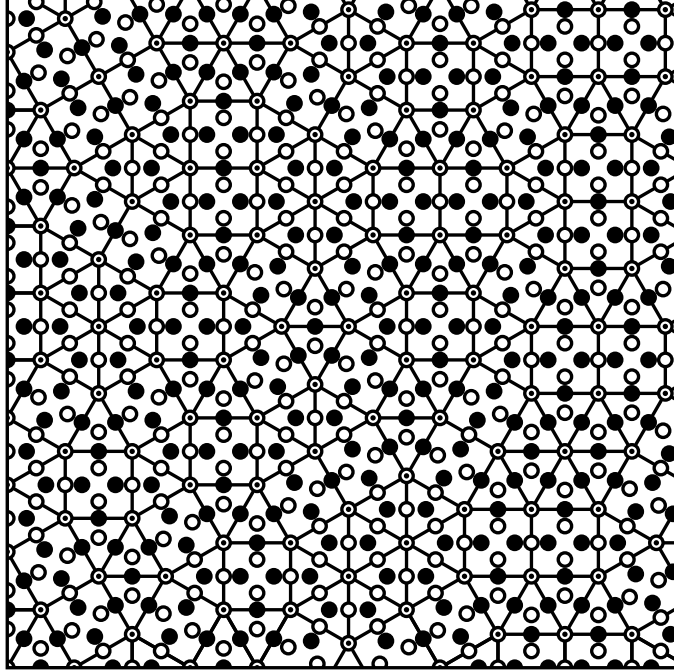


FIG. 3. Patch of a decorated square-triangle quasicrystal. The dotted atoms are at  $z = 1/4$  and  $3/4$  in the  $A$  layer, the white atoms are at  $z = 0$  in the  $B$  layer and the black atoms at  $z = 1/2$  in the  $\bar{B}$  layer.

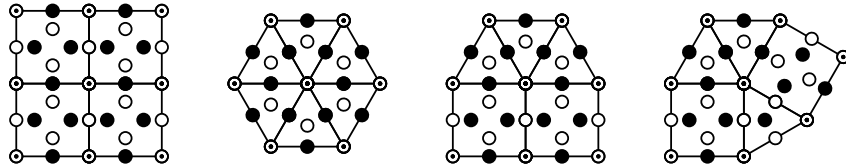
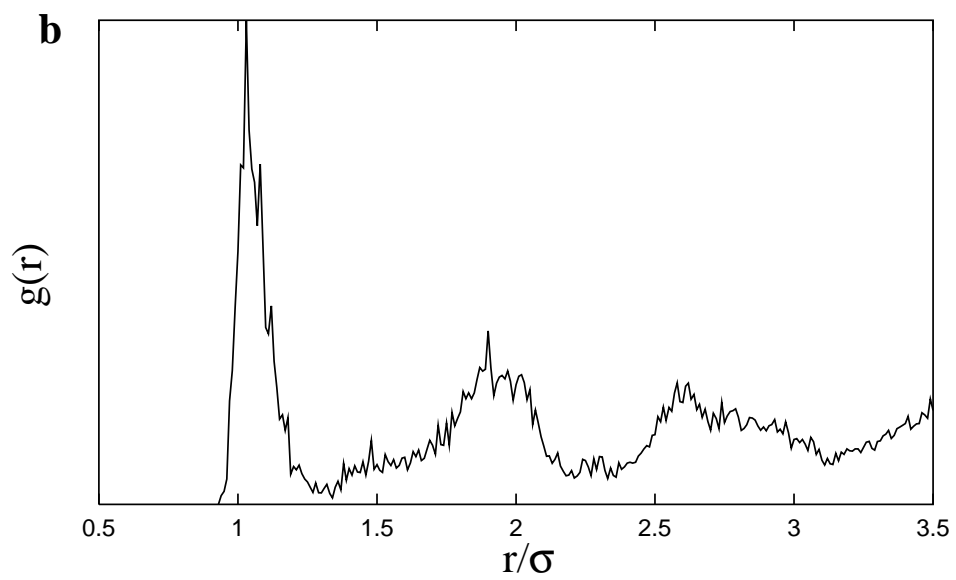
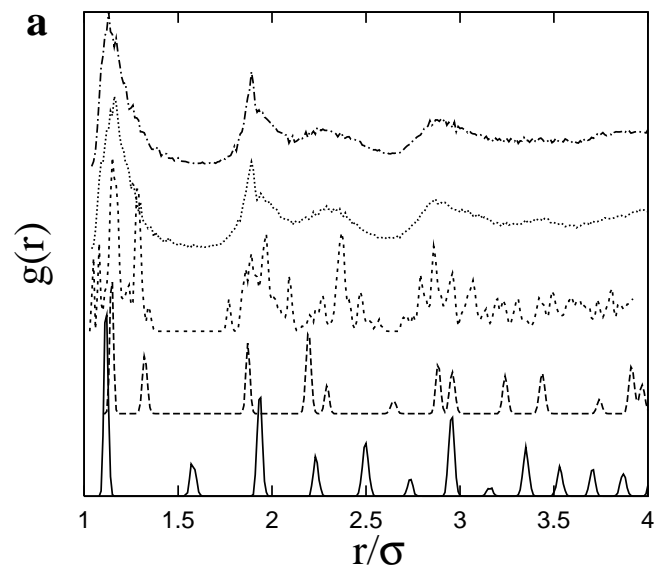


FIG. 4. Vertex configurations of the crystalline phases with a single vertex configuration. From left to right: A-, Z-, H- and  $\sigma$ -phase or a, z, h, and  $\sigma$  vertex, respectively.



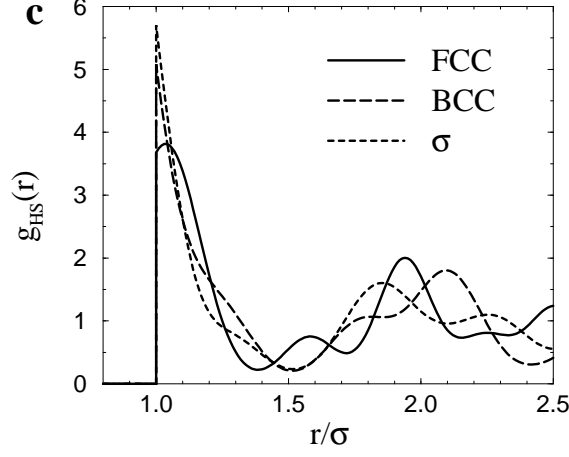


FIG. 5. Radial distribution functions for various systems. (a) From bottom to top: fcc, bcc,  $\sigma$ -phase, tcp-phase, amorphous phase. The samples have been expanded to  $P\sigma^3/\epsilon = 0.001$  and quenched to  $T = 0$ . Vertical scale is in arbitrary units, all curves being scaled to the same maximum. (b) A sample obtained from cooling at  $P\sigma^3/\epsilon = 25$  and  $k_B T/\epsilon = 0.75$ . The shoulder at  $r = 1.5 \sigma$  indicates the onset of a transition to fcc; (c) Hard-sphere solid at reduced density  $\rho\sigma^3 = 1.0$ , computed from Eqs. (13)-(15): fcc crystal (solid curve), bcc crystal (long-dashed curve), and  $\sigma$ -phase (short-dashed curve).

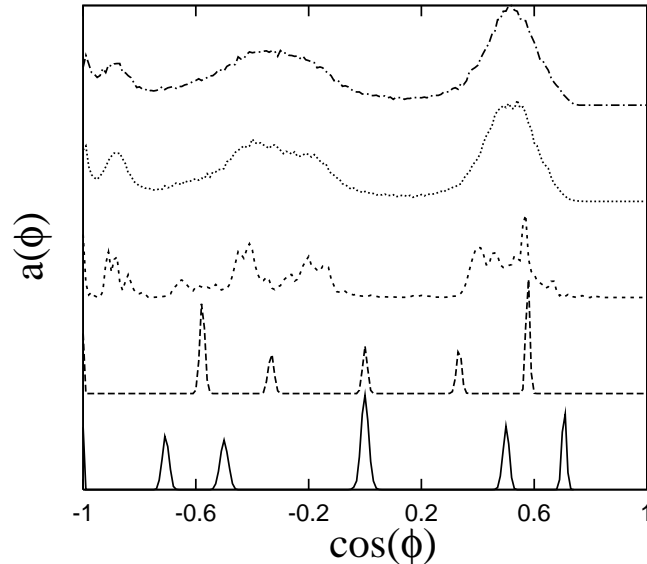
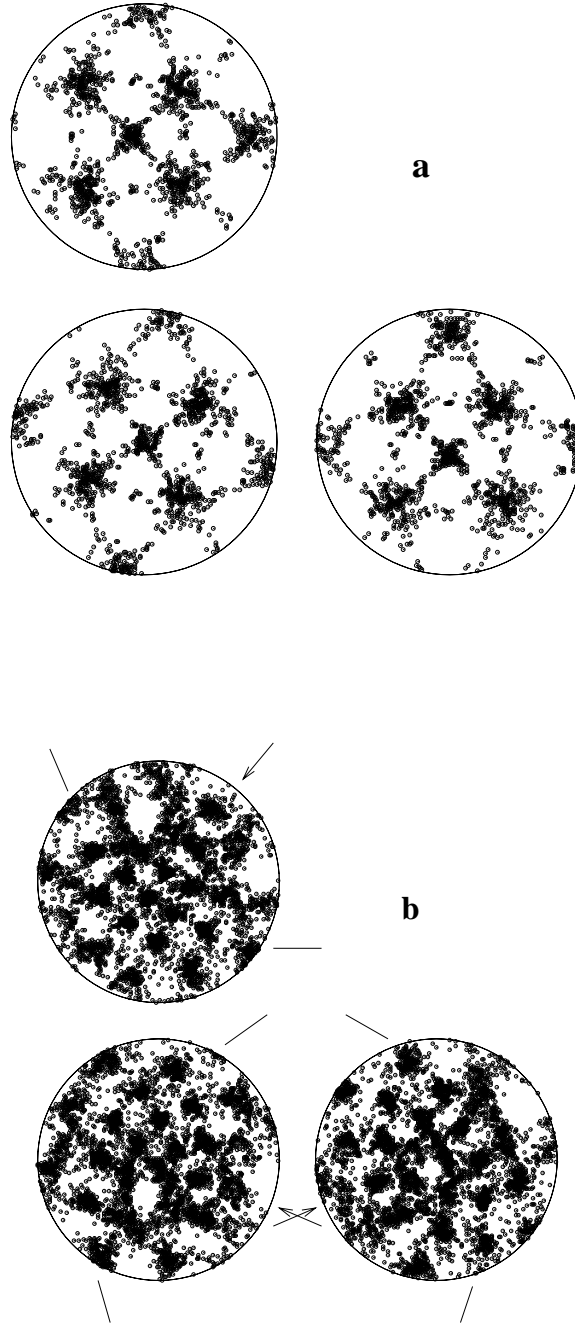


FIG. 6. Angular distribution functions. From bottom to top: fcc, bcc,  $\sigma$ -phase, tcp-phase, amorphous phase. The samples have been expanded to  $P\sigma^3/\epsilon = 0.001$  and quenched to  $T = 0$ .



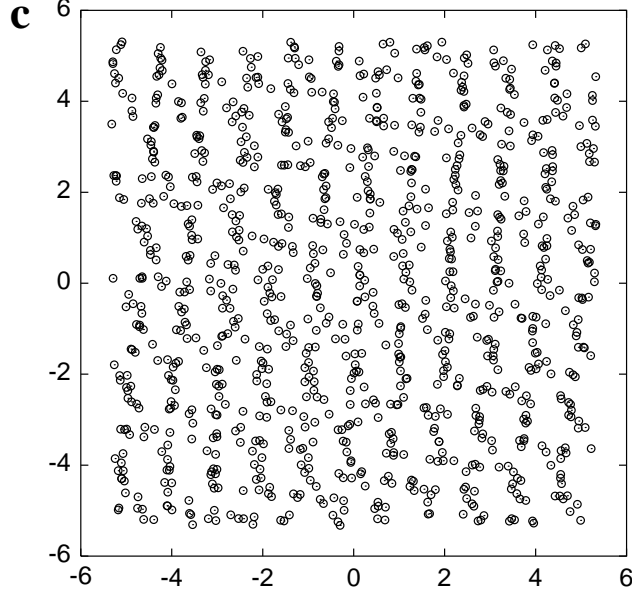
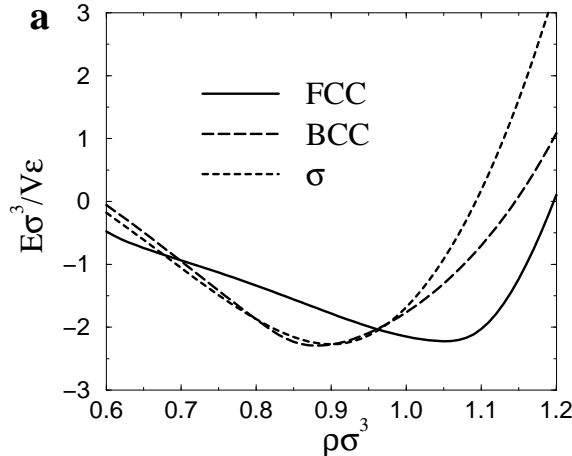


FIG. 7. (a) Spherical projection of the nearest-neighbor vectors of a non-perfect bcc sample generated by cooling. Three views of the sphere along perpendicular directions are given; (b) Spherical projections of the nearest-neighbor vectors of a tcp sample obtained by cooling. Three perpendicular views are given. The poles of the sphere are marked by arrows, and the equator is indicated with dashes. The six maxima along the equator represent the twelve-fold symmetry; (c) Projection of a tcp sample obtained by cooling at  $P\sigma^3/\epsilon = 3.5$  and  $k_B T/\epsilon = 0.55$ . The sample has been expanded to  $P\sigma^3/\epsilon = 0.001$  and quenched to  $T = 0$  after nucleation.



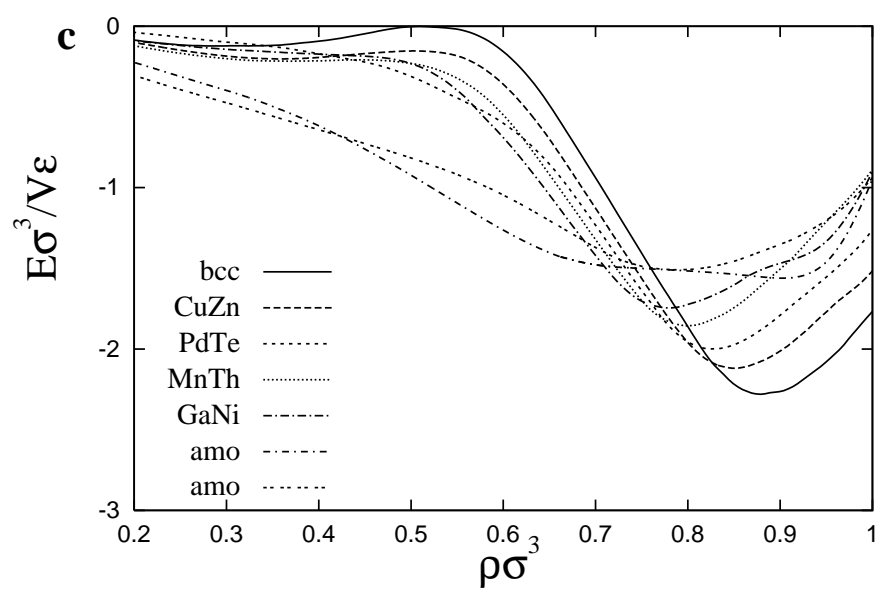
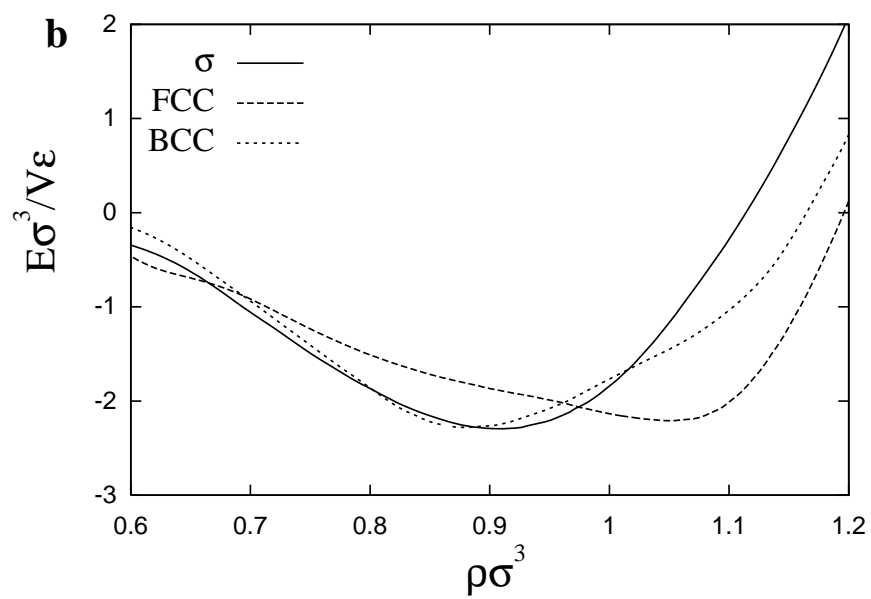


FIG. 8. Ground-state energy per unit volume vs. density, in reduced units. (a) Results of lattice summation of the Dzugutov pair potential for ideal fcc crystal (solid curve), bcc crystal (long-dashed curve), and  $\sigma$ -phase (short-dashed curve); (b) Results of MD simulation, with structural relaxation, for  $\sigma$ -phase (solid curve), fcc (long-dashed curve), and bcc (short-dashed curve); (c) MD simulation data for the bcc vacancy phases and the low density amorphous structures. The lowest minimum at the right is bcc followed by  $\text{Cu}_5\text{Zn}_8$ ,  $\text{Pd}_{4-x}\text{Te}$ ,  $\text{Mn}_{23}\text{Th}_6$ , and  $\text{Ga}_4\text{Ni}_3$ . The next minimum belongs to the amorphous phase formed from  $\text{NiTi}_2$ . The remaining double-dashed curve is the amorphous phase generated by cooling the melt.

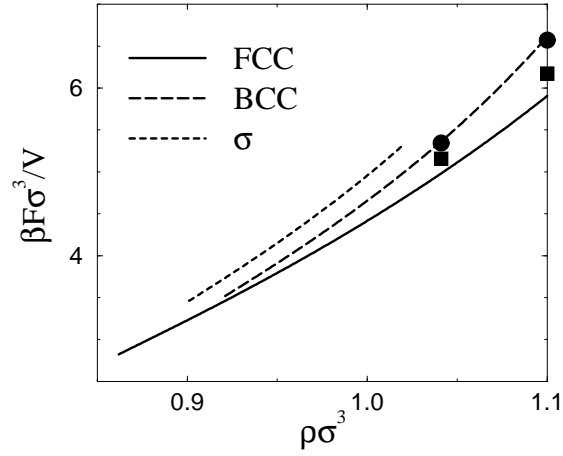


FIG. 9. Free energy per volume vs. density, in reduced units, for the reference hard-sphere solid, computed from Eqs. (6), (9), and (12). Curves have the same meaning as in Fig. 8a. Circular and square symbols are Monte Carlo simulation data, from Ref. [19], for hard-sphere bcc and fcc crystals, respectively.

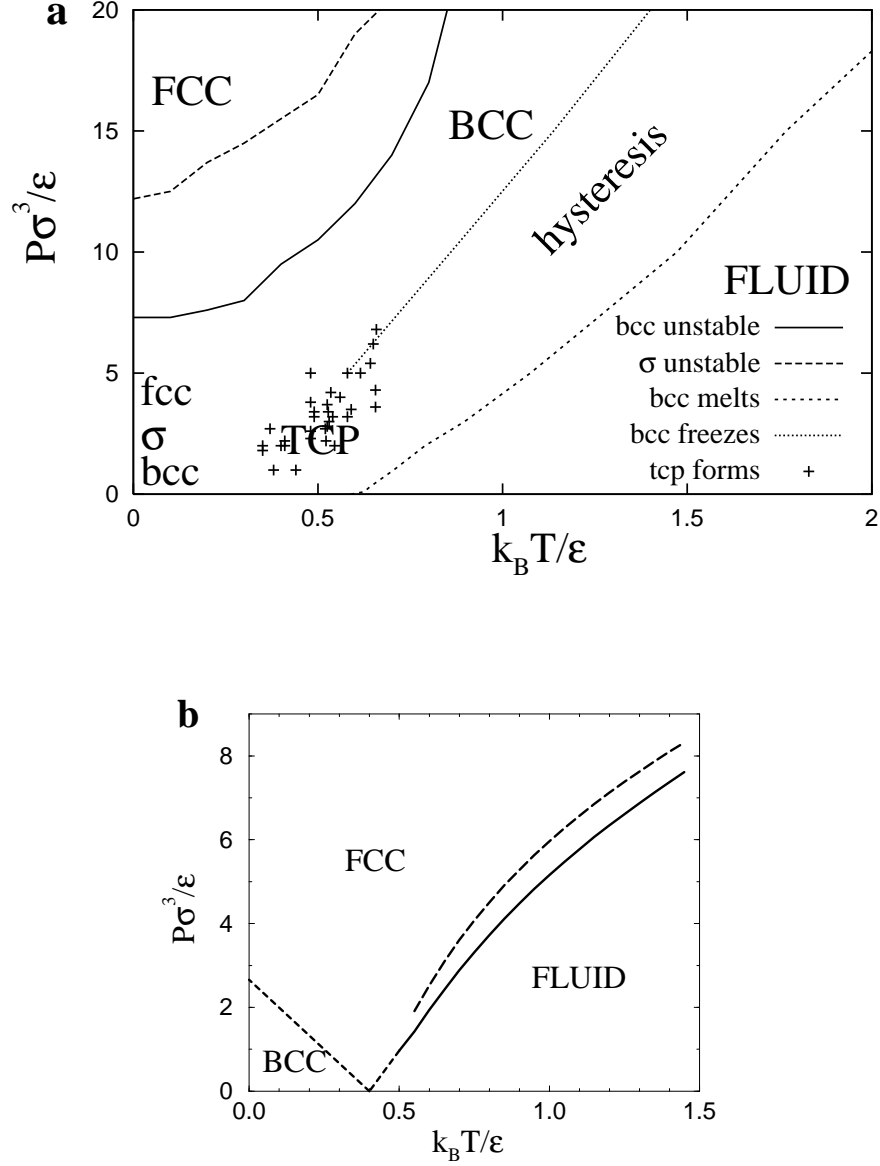


FIG. 10. Pressure-temperature phase diagram. (a) MD simulation results: The instability lines denote boundaries where respective structures are destabilized if compressed to high pressures. Capital letters mark phases formed by cooling simulations, lowercase letters phases obtained by ground-state structure calculations. Crosses characterize region where tcp-phase is found in cooling simulations. The region between the melting/expansion transition line and the cooling/compression transition line is the hysteresis region; (b) Perturbation theory predictions: Phase boundaries are shown between fluid and fcc crystal (solid curve) and between fluid and metastable bcc crystal (long-dashed curve). Short-dashed curves are postulated extrapolations to low  $P$  and  $T$ .



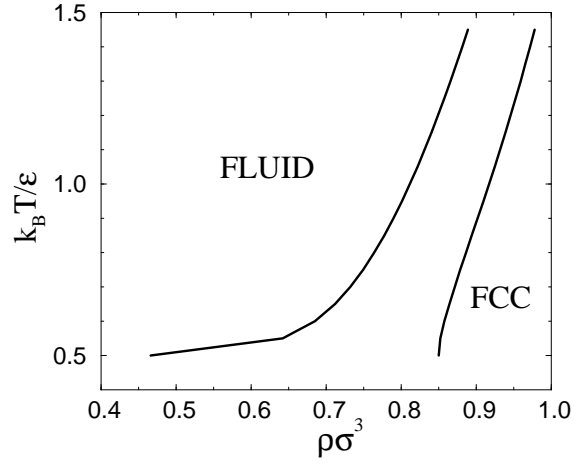


FIG. 11. Predictions of perturbation theory for the fluid-solid phase diagram in the temperature-density ( $T-\rho$ ) plane. For  $k_B T/\epsilon > 0.5$ , theory predicts the fcc crystal to be the only stable solid phase.